nature communications

Article

https://doi.org/10.1038/s41467-024-52354-x

A bioabsorbable mechanoelectric fiber as electrical stimulation suture

Received: 6 March 2024

Accepted: 3 September 2024

Zhouquan Sun[1,6], Yuefan Jin[2,6], Jiabei Luo[1], Linpeng Li[2] ✉, Yue Ding[3], Yu Luo[4], Yan Qi[5], Yaogang Li[1], Qinghong Zhang[1], Kerui Li[1], Haibo Shi[2], Shankai Yin[2], Hongzhi Wang[1] ✉, Hui Wang[2] ✉ & Chengyi Hou[1] ✉

In surgical medicine, suturing is the standard treatment for large incisions, yet traditional sutures are limited in functionality. Electrical stimulation is a non-pharmacological therapy that promotes wound healing. In this context, we designed a passive and biodegradable mechanoelectric suture. The suture consists of multi-layer coaxial structure composed of (poly(lactic-co-glycolic acid), polycaprolactone) and magnesium to allow safe degradation. In addition to the excellent mechanical properties, the mechanoelectrical nature of the suture grants the generation of electric fields in response to movement and stretching. This is shown to speed up wound healing by 50% and reduce the risk of infection. This work presents an evolution of the conventional wound closure procedures, using a safe and degradable device ready to be translated into clinical practice.

Acute and chronic surgical wounds are prevalent in clinical practice worldwide[1]. Millions of people require varying levels of therapy each year, ranging from basic wound care to internal repair[2]. Especially for incisional wounds caused by trauma or surgery, it is crucial to completely seal the opened tissue to facilitate the healing process and minimize complications, including infection and inflammation. Historically, suture fibers have been the primary medical device used for wound closure[3–5]. Currently, the basic requirement for sutures used in clinical surgery is that they are bioabsorbable, as this avoids damage to the healing site from secondary suture removal[6,7]. However, despite the fact that synthetic absorbable sutures are biocompatible and cause minimal tissue reaction, they still fail to accelerate wound healing to reduce the risk of infection.

The reported intelligent sutures are almost designed to accelerate wound healing by surface-loading drugs or growth factors for slow-release therapy[8,9]. However, most drugs either exert insignificant effects on wound healing or cause serious side effects such as allergies and nausea[10]. Simultaneously, growth factor-mediated therapy faces the challenge of being susceptible to contamination, inactivation and degradation[11]. In addition, other reported intelligent sutures are mostly used for sensing and monitoring the recovery of the wound site and have no therapeutic capability[12]. In contrast, electrical stimulation (ES) has been proven to be an effective strategy for wound care in non-pharmacological therapies, since it mimics the natural healing mechanism of endogenous electric field[13]. ES promotes the migration of Na^+/K^+ between tissues, stimulates the production and reception of growth factors, directs the neurite growth, and further induces cell migration and proliferation[14].

Typically, active electrical stimulation devices have limitations in wound therapy due to the need for an external power source[15]. On the contrary, state-of-the-art self-powered ES devices which were prepared on the basis of triboelectric[16–18] and piezoelectric[19,20] effects have been

---

[1]State Key Laboratory for Modification of Chemical Fibers and Polymer Materials, College of Materials Science and Engineering, Donghua University, Shanghai, P. R. China. [2]Shanghai Key Laboratory of Sleep Disordered Breathing, Department of Otolaryngology-Head and Neck Surgery, Otolaryngology Institute of Shanghai JiaoTong University, Shanghai Sixth People's Hospital Affiliated to Shanghai Jiao Tong University School of Medicine, Shanghai, P. R. China. [3]Department of General Surgery, Tongji Hospital, Tongji University Medical School, Shanghai, P. R. China. [4]Shanghai Engineering Research Center of Pharmaceutical Intelligent Equipment, Shanghai Frontiers Science Research Center for Druggability of Cardiovascular Non-coding RNA, Institute for Frontier Medical Technology, School of Chemistry and Chemical Engineering Shanghai University of Engineering Science, Shanghai, P. R. China. [5]Yangzhi Rehabilitation Hospital Affiliated to Tongji University, Tongji University School of Medicine, Shanghai, P. R. China. [6]These authors contributed equally: Zhouquan Sun, Yuefan Jin. ✉e-mail: lilp@sjtu.edu.cn; wanghz@dhu.edu.cn; wangh2005@alumni.sjtu.edu.cn; hcy@dhu.edu.cn

widely reported, and these devices significantly accelerated wound healing. Nevertheless, these ES devices are almost two- or three-dimensional[21–24] and mainly targeted for microtrauma[25,26], nerve[27,28] or bone repair[29,30], etc., and cannot be applied in the face of an injury site that requires suturing, e.g., large incisions. In addition, Part of the devices cannot be degraded and absorbed in human body system[31,32]. On the other hand, producing one-dimensional bioabsorbable ES sutures remains a challenge because (1) one-dimensional devices commonly face interfacial problems since they usually perform large deformations to generate sufficient electrical output[33–35], and (2) degradable materials are difficult to process on a one-dimensional scale due to brittleness issues[36,37]. Therefore, the creation of cutting-edge intelligent medical sutures would further advance the field of biomedicine.

Here, we developed a continuous, bioabsorbable core-sheath structured mechanoelectric fiber as an electrical stimulation suture (BioES-suture). The design of fibrous structure which consists of biodegradable polymers (poly(lactic-co-glycolic acid), polycaprolactone) and resorbable metal (magnesium) enables BioES-suture to be degraded and resorbed in living organisms after completing its therapeutic work. BioES-suture could generate sufficient ES at the site of wound injury through natural movement to aid cell proliferation and migration, accelerating wound healing. Moreover, we verified the behavior of wound accelerated healing under electrical stimulation by scratch assays in vitro and rat muscle wound experiments in vivo, and a corresponding possible mechanism for accelerated wound repair was proposed. This work provides an advanced solution for the creation of intelligent surgical sutures.

Results

Overview concept and material design of the bioabsorbable electrical stimulation suture

Skin and muscle cover almost the whole body, and their postoperative repair is crucial in clinical surgery[25]. Especially when dealing with internal postoperative gashes, patch-type electrical stimulation devices cannot provide effective wound closure and can only be treated by suturing (Fig. 1a). We demonstrated the unique usefulness of electrical stimulation suture by comparing it with other state of the art therapeutic devices (Supplementary Table 1). For such gashes in vivo, the desired recovery process is as follows: the wound is tightly closed by using a suture, while the suture can provide electrical stimulation (ES) to accelerate the wound repair by promoting tissue regeneration, ECM deposition and vascularization, and the suture can be degraded and absorbed in vivo after the recovery. To address these needs, we designed a completely bioabsorbable mechanoelectric fiber as electrical stimulation suture (BioES-suture). The suture consists of a core-sheath structure: the core layer is a bioabsorbable PLGA nanofiber-wrapped Mg filament, and the sheath layer is a biodegradable thermoplastic material, PCL. The suture generated electrical energy through triboelectric mechanism during contraction-diastole process of muscle, which created an electric field at the wound for ES.

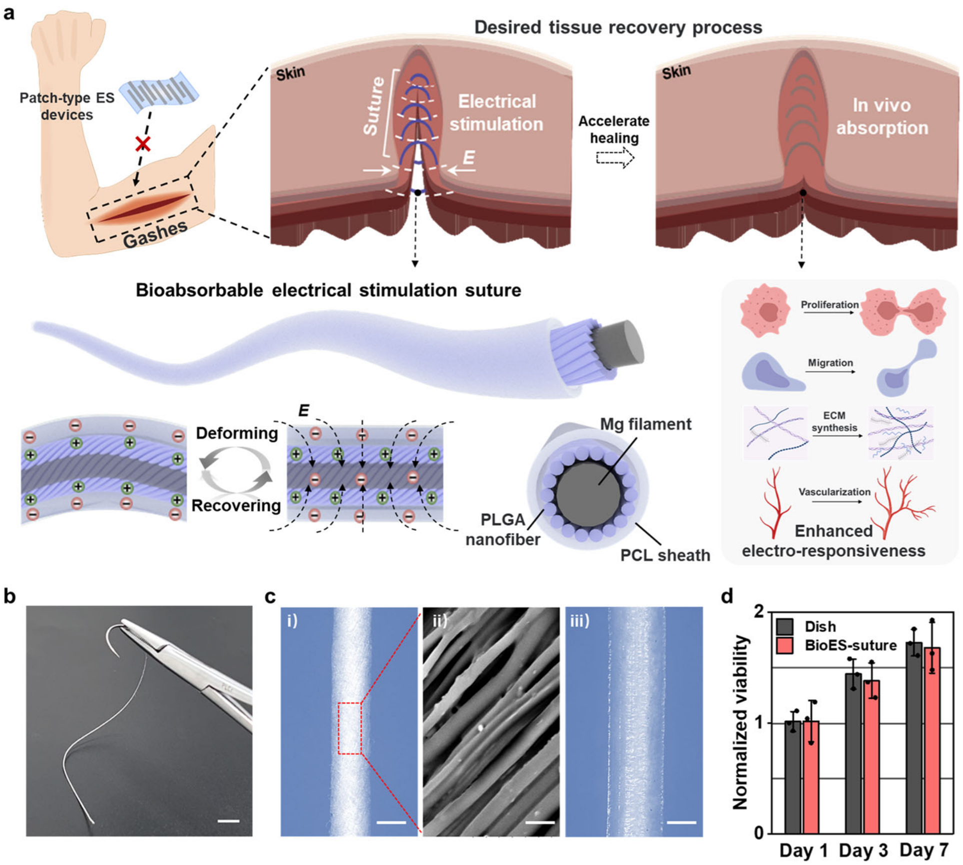

Fig. 1 | Overview concept and material design of the bioabsorbable electrical stimulation suture (BioES-suture) for treating muscle gashes. a The desired tissue recovery process when treating the gashes, including suturing the wound, electrical stimulation to accelerate healing, and in vivo absorption of suture. The BioES-suture generated electric field through the muscle deformation at the wound for electrical stimulation. Accelerated wound healing by promoting tissue regeneration, ECM deposition and vascularization under the synergistic effect of mechanical suturing and electrical stimulation. **b** A photo of the BioES-suture. Scale bar: 2 cm. **c** The mciroscale morphology of the (i) pre-assembled core fiber, (ii) PLGA nanofibers and (iii) BioES-suture. Scale bar: 250 μm in optical photographs and 2 μm in scanning electron microscope (SEM) image. **d** Comparison of normalized cell viability for 7 days showing excellent biocompatibility of the BioES-suture. $n = 3$ independent samples for each group, data represent mean ± standard deviation.

BioES-suture can be prepared by a continuous process (Supplementary Fig. 1a). First, PLGA nanofibers were twisted onto the surface of Mg filament electrode using Fermat spinning to form pre-assembled core fiber (Mg@PLGA). Subsequently, we extracted the pre-assembled core fiber from the PCL melt using a modified melt-spinning method (Supplementary Note 1). As a result of the low melting point of PCL (~65 °C), it can be rapidly cooled in air and wrapped around the pre-assembled core fiber to obtain the BioES-suture. The photographs and microscopic morphology of the BioES-suture are illustrated in Fig. 1b and c and Supplementary Fig. 1b, the diameters of the BioES-suture and PLGA nanofibers are 354 ± 12 µm and 500–1000 nm, respectively. The thickness of the PLGA layer was calculated from the diameter of the pre-assembled core fiber (Mg@PLGA) minus the diameter of the Mg filament and was 67 ± 10 µm. The thickness of the PCL was calculated from the diameter of the BioES-suture minus the diameter of the pre-assembled core fiber and was 87 ± 10 µm. The PLGA nanofiber layer and the PCL melt-spinning layer constitute the power generation unit. Among them, the Fermat twisted nanostructures can provide high specific surface area for the pre-assembled core fiber to enhance the triboelectric performance of the suture. Meanwhile, the Mg filament serves as the electrical energy harvesting unit to provide electrical stimulation.

We further measured the strength of the BioES-suture to prove that it could achieve the requirements for suture. Compared with commercial sutures, including both bioabsorbable and non-absorbable sutures, the BioES-suture has a higher tensile strength (265 MPa, Supplementary Fig. 2a-d). In addition, BioES-suture prepared by using PLGA with different monomer ratios and PCL with different molecular weights all possessed a tensile strength of more than 250 MPa (Supplementary Fig. 2e,f). After bending BioES-suture for 1000 times, the strength was maintained at 239 MPa and elongation at break was 9.8%, and this high strength and low strain proved that it had good suturing properties (Supplementary Fig. 2g). In addition, we have demonstrated through comparison and optimization of dielectric materials that the triboelectric fibers consisting of PLGA and PCL exhibits the optimal electrical performance (Supplementary Fig. 3).

In order to demonstrate that BioES-suture can be used as an implantable device, we tested the biocompatibility of the constituent materials. Sheared Mg filaments, Mg@PLGA fibers and BioES-suture were used to culture fibroblasts (L929), respectively. The biocompatibility of BioES-suture was assessed by comparing the morphology and proliferation of fibroblasts cultured for 7d in the experimental and control groups (standard petri dishes). Similar densities were observed for consecutive 7 days of cell culture (Supplementary Fig. 4a,b). Cell Counting Kit-8 (CCK-8) method was used to characterize the viability of L929 cells in each group (Fig. 1d and Supplementary Fig. 4c)[38]. The relative viability of the three groups was not significantly different from that of the control group when compared to the normalized reference value in the culture dish (above 90% within 7 days). The normal spreading and non-stagnant proliferation of fibroblasts demonstrated the non-toxicity and biocompatibility of BioES-suture.

Electrical performance and degradative characteristics of the BioES-suture

Since BioES-suture exists in the body fluid microenvironment after implantation, we measured the power generation performance of BioES-suture in the liquid medium (Fig. 2a). BioES-suture was wound onto an artificial muscle fiber (polyurethane elastomer with 0.5 cm diameter) and tightly adhered to this fiber, preventing the contact-separation of the suture from the fiber to interfere with the triboelectric output. The electrical output of BioES-suture was measured by subjecting the fiber to a stretch-recovery step to simulate muscle contraction-diastole. The combined device was placed underwater to generate electricity by inducing a potential difference of contact-separation between the PLGA nanofiber and the PCL sheath in the suture during the stretch-recovery process (triboelectric effect) (Supplementary Fig. 5a). The electrical output of the BioES-suture could light up an LCD screen (Supplementary Movie 1). We compared the electrical output of BioES-suture in air and underwater. As shown in Fig. 2b, the output voltage increases by 1.39 V underwater than in air, which is due to that the surface potential from triboelectrification induces the polarization of surrounding bulk water to increase the amount of friction charge generated (Supplementary Fig. 5b,c)[39]. It is also noteworthy that even at small tensile strains (10 %), the BioES-suture can still generate output voltages in excess of 2 V (Supplementary Fig. 6a), which is highly favorable for implantable electrical stimulation devices. This sensitive power generation property stems from improvements to melt-spinning (Supplementary Note 1), which allows for a narrower gap between the PCL sheath and the PLGA nanofibers (Supplementary Fig. 6b), and the PLGA nanofibrous structure is not disrupted due to the low melting point of the PCL than that of PLGA. Following this, we systematically measured the electrical properties at different frequencies. The output voltage of the BioES-suture remains stable (~5.6 V) at different frequencies (Supplementary Fig. 6c).

For electrical stimulation of wound healing, negative charges tend to promote cellular gene expression more than positive charges[29]. We measured the surface potential of the PCL sheath before and after contact with PLGA by using Kelvin Probe Force Microscopy (KPFM) (Fig. 2c). The surface potential of the PCL decreased by 117.2 mV from 51.8 mV to −65.4 mV, suggesting that electrons are transferred from the PLGA nanofibers to the PCL sheath after friction, and thus negative potential stimulation can be generated in the electrode. We further developed a model of muscle stitching to illustrate the trend of the EF due to the negative potentials generated by BioES-suture. The direction of the EF generated by the BioES-suture is consistent with the direction of the endogenous EF to generate an EF from the intact tissue around the wound to the wound site (Supplementary Fig. 7). In addition, COMSOL simulation results showed that BioES-suture could generate an electric field of more than 100 mV/mm in the direction from the surrounding normal muscle to wound within the suture region (Fig. 2d, Supplementary Fig. 8). Therefore, the BioES-suture could implement stable and effective electric field stimulation into the wound when sutured around the gash area[40].

The in vitro degradation behavior of BioES-suture was then investigated. The Mg electrode and BioES-suture were immersed in phosphate-buffered saline solution (PBS, pH 7.4) and placed in a constant temperature oscillating incubator for degradation (Supplementary Fig. 9a)[41]. The degradation mechanism of each component is shown in Supplementary Fig. 9b. The Mg electrode and pre-assembled core fiber (Mg@PLGA nanofibers) were completely destroyed within 14 days (muscle recovery period)[42], whereas there were no obvious etching traces on the surface of the BioES-suture (Fig. 2e and Supplementary Fig. 9c), indicating that PCL could serve as a good protective layer during the muscle recovery period. After 24 weeks of degradation, no obvious BioES-suture could be observed in PBS (Supplementary Fig. 9d). For the electrical properties of BioES-suture during the degradation period, it exhibited a stable electrical output of about 2.8 V within 14 days (Supplementary Fig. 10a). After 13 weeks of degradation, BioES-suture lost its electrical generation performance, which was attributed to the fact that a portion of the PCL sheath on the surface was degraded and etched, and water penetrated into the interior of BioES-suture, causing it to lose triboelectrification capability (Supplementary Fig. 10b,c). We further conducted cytotoxicity tests in vitro using the degradation solution of Mg electrode and BioES-suture to verify the biocompatibility of the degradation products. As shown in Supplementary Fig. 11, there

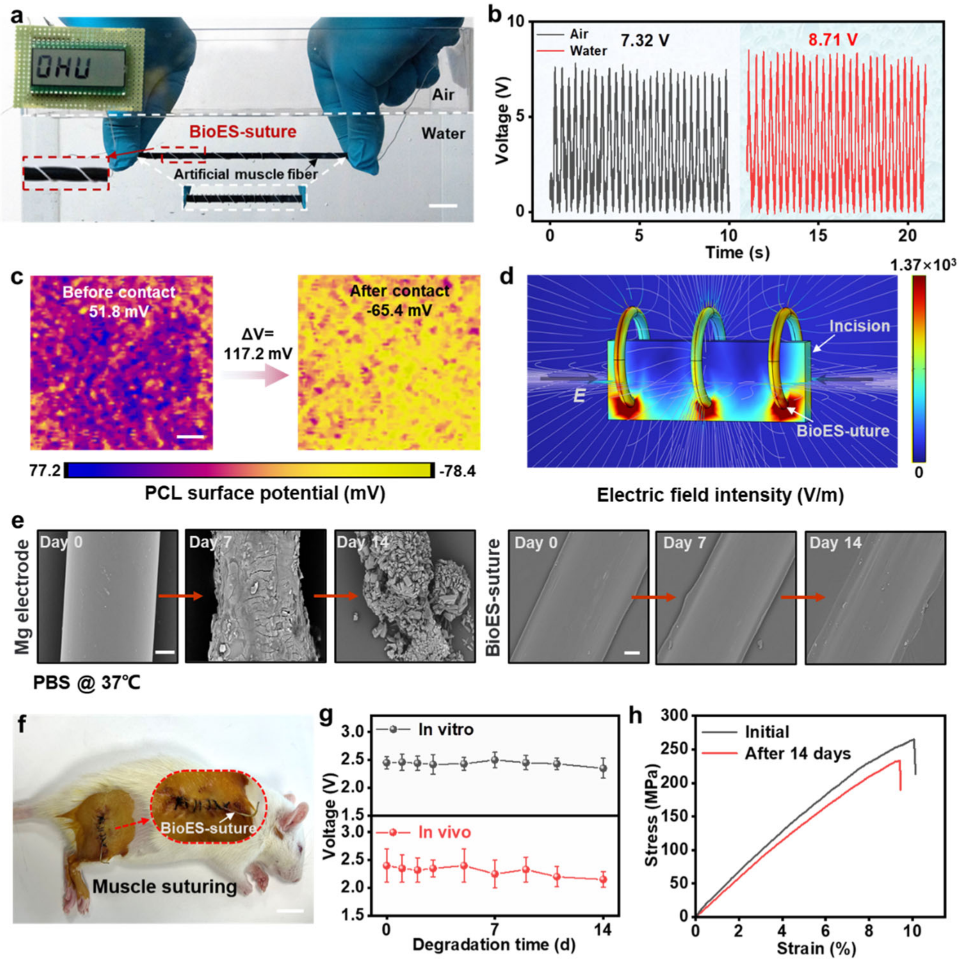

Fig. 2 | Electrical performance and degradative characteristics of the BioES-suture. a Side view of the experimental setup to measure the output performance of the BioES-suture (white color) in water. Scale bar: 2 cm. **b** Voltage output of the BioES-suture measured in air and water, respectively. **c** KPFM images describing the difference in surface potential of the PCL layer before and after contact with PLGA layer. **d** COMSOL simulation of the distribution of the electric potential generated by the suture at the wound site. The circles represent BioES-sutures, the rectangle represents the incision and the white lines represent the EF of the BioES-suture. **e** SEM images of the natural degradation process of Mg electrode and BioES-suture during the muscle recovery period. Scale bar: 40 μm. **f** Optical image of the BioES-suture at the implanted site of an SD rat (red dotted frame). Scale bar: 3 cm. **g** Voltage output recorded from the BioES-suture in vitro (top) and in vivo (bottom) for 14 days, respectively. $n = 3$ independent samples, data represent mean ± standard deviation. (h) Tensile strength of the BioES-suture before and after implantation for 14 days.

was no significant statistical difference in the proportion of live cells (green) in the experimental group treated with the degradation solutions of Mg electrode (91.3 %) and BioES-suture (92.7 %) compared to the control group (93.8 %). This demonstrates that the degradation products of BioES-suture are not significantly toxic to cell growth.

BioES-suture was further sutured into the leg musculature of rats to monitor their power generation capacity in vivo (Fig. 2f). During the muscle recovery period, the voltage output of the BioES-suture at normal activity of the rat was shown in Supplementary Fig. 12. It was revealed that the output voltage value during normal exercise in rats was about 2.3 V, which was similar to the output induced by the in vitro simulation (stretching 10 %) (Fig. 2g). This comparison confirms that our BioES-suture can effectively convert random body movements into stable electrical impulses. After 14 days, the implanted BioES-suture was removed and its strength was measured to be 234 MPa, still maintaining more than 90 % of its initial strength (Fig. 2h). All of these results indicate that the BioES-suture can be used for muscle suturing and can provide adequate sewing strength and electrical stimulation during the muscle recovery period.

Assessment of the effects of electrical stimulation on behaviors of fibroblasts

Next, we established an in vitro wound model to assess the effectiveness of ES that was produced by BioES-suture in promoting simulated wound healing (referred to as the BioES group) (Fig. 3a and Supplementary Fig. 13)[43]. NIH 3T3 fibroblasts were chosen as the model cell line since fibroblasts play a crucial role in wound migration and tissue remodeling. For the BioES group, the electrical signal which was generated by BioES-suture provided continuous and stable ES to the stimulation electrode at the bottom of the petri dish, and no ES was applied to the control group. In the BioES group, efficient migration of NIH 3T3 cells could be achieved within 24 h, which was significantly faster than that of the control group (Fig. 3b and Supplementary Fig. 14). Quantitative analysis also confirmed that the cells exposed to ES exhibited a significantly higher rate of migration (Fig. 3c). Image J was used to calculate the cell-free area in the microscope images. The original relative wound area was approximately 69.3%, but 24 h later, due to the imposed ES effect, the cells in the BioES group migrated faster, with a wound coverage of approximately 10.8 % compared to 32.6 % in the control group (Fig. 3d).

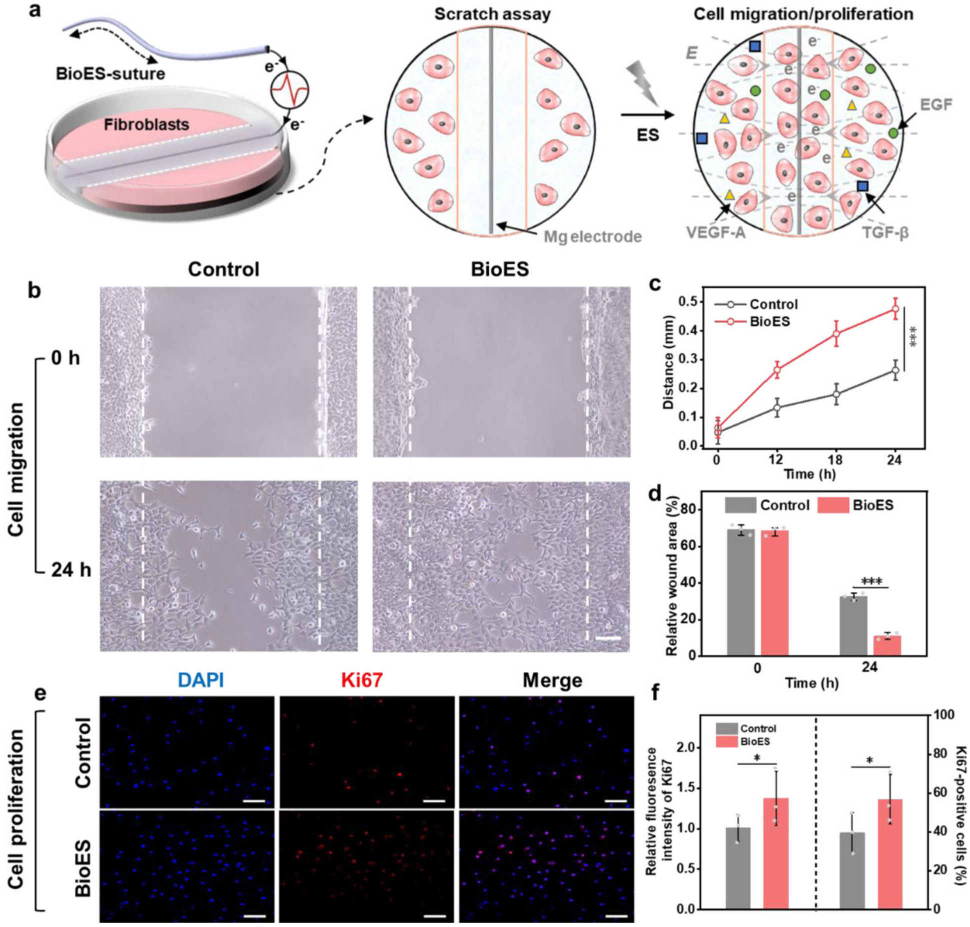

Fig. 3 | Assessment of the effects of electrical stimulation on behaviors of fibroblasts. **a** Schematic diagram of BioES-suture generating ES to promote cell migration and proliferation. **b** Microscopic images of the scratch assay. The cells were stimulated with or without ES. The cells were stimulated for 1 h, and images from two group were captured 24 h later. Scale bar: 100 µm. **c** Cell migration distances at different time points after performing the scratch assay. n = 3 independent samples. (d) Relative wound area from the group with and without ES in the scratch assay. n = 3 independent samples. (e) The immunofluorescence images of Ki67-stained fibroblasts show the proliferation status of two groups. The cells were stimulated for 1 h at 12 h intervals and were captured 72 h later. Scale bar: 100 µm. (f) The relative fluorescence intensity of Ki67 and proportion of Ki67-positive cells in each group. All statistical analyzes were performed by one-way ANOVA, data represent mean ± standard deviation, $^{*}p < 0.05$, $^{***}p < 0.001$.

Furthermore, the proliferation of fibroblasts in the BioES group and the control group was investigated. The same concentration of cells was cultured in the two experimental setups. After 72 hours of incubation, we performed immunofluorescence staining for Ki67 (Fig. 3e) and quantified the proportion of Ki67-positive cells and the relative fluorescence intensity of Ki67 in each group (Fig. 3f). The cell nuclei were stained with 4′,6-diamidino-2-phenylindole (DAPI) and examined using confocal laser scanning microscopy (CLSM). The results indicated that the BioES group had a significantly higher proportion of Ki67-positive cells (56.8%) and relative fluorescence intensity of Ki67 compared to the control group (39.5%). This suggests that BioES-suture enhanced cell proliferation, thereby promoting wound healing. In addition, CCK-8 was used to detect the absorbance at 450 nm at different time points. With the increase of stimulation duration, the variation in absorbance between the two groups became more significant, indicating enhanced cell viability and proliferation (Supplementary Fig. 15). The changes in cell metabolism were further detected by ELISA assay. Three growth factors, including epidermal growth factor (EGF), vascular endothelial growth factor-A (VEGF-A), and transforming growth factor-beta (TGF-β), were tested in the supernatants of cell culture solutions at 24 h, 48 h, and 72 h after applying the ES, respectively (Supplementary Fig. 16). Compared with the control group, the expression of the three growth factors was significantly enhanced in the cells of the BioES group. As a conclusion, the results of the in vitro trauma model suggest that the electrical output generated by BioES-suture can be applied by stimulating (Mg) electrodes on the injured tissue. This electrical stimulation can accelerate cell migration and proliferation by promoting the expression of growth factors and thus providing a strong contractile force for acute wound healing.

We further conducted in vitro experiments to verify the antibacterial capabilities of the sutures by immersing ordinary surgical sutures (control group), BioES-suture (Bio group) and electricity-producing BioES-suture (BioES group) in Staphylococcus aureus and Escherichia coli cultures for 24 h. After incubation, these sutures were stained with Calcein-AM/PI dyes to label live bacteria (green) and dead bacteria (red), thus verifying the in vitro bacterial inhibition capabilities of the different groups (Supplementary Fig. 17a). The relative fluorescence intensity of dead S. aureus and E. coli on BioES-suture showed no significant statistical difference compared to the ordinary surgical sutures (Supplementary Fig. 17b). However, electricity-producing BioES-suture exhibited a significant inhibitory effect on bacterial growth, suggesting that the electrical stimulation provided by the BioES-suture has the potential to provide an antimicrobial effect during the wound healing process.

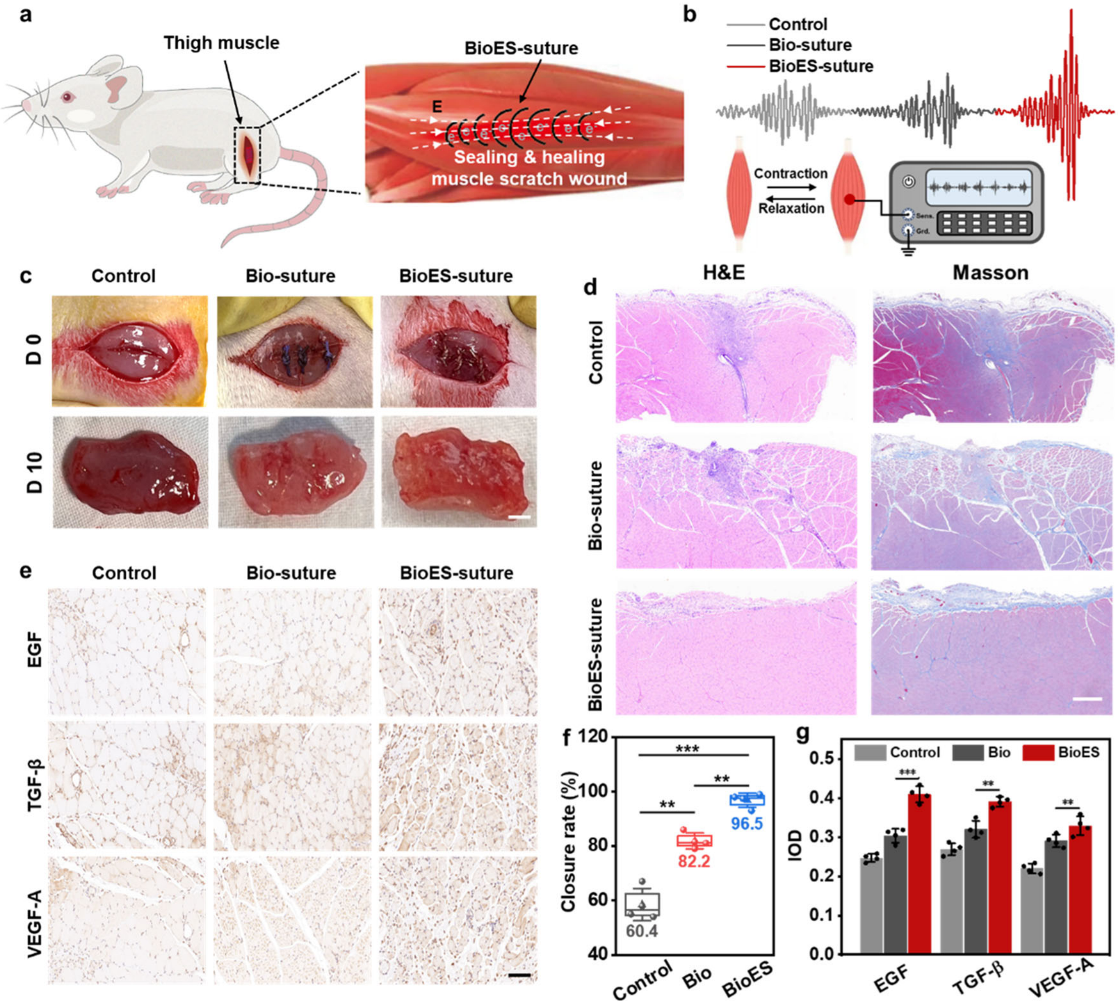

Fig. 4 | Verification of BioES-suture in accelerating wound healing in vivo. **a** Schematic showing how BioES-suture promoted muscle wound healing. **b** Comparison of electromyography (EMG) signals in three groups. Including the unsutured (control) group, the bioabsorbable suture (Bio-suture) group and the BioES-suture group. **c** Representative optical images of wound areas after 10 days of recovery in each group. Scale bar: 500 µm. **d** H&E and Masson staining images of tissue sections the wounds and adjacent muscle areas. Scale bar: 100 µm. **e** Immunohistochemistry staining images of multiple growth factors including EGF, TGF-β, and VEGF-A. Scale bar: 100 µm. **f** Analysis of the wound closure rate after 10 days of recovery in each group. $n = 4$ independent samples. The box represents the 25–75% confidence interval, the triangle represents the mean, the error bars represent the standard deviation, and the horizontal line in the box represents the median. **g** Immunofluorescence score of the various growth factors expressed in each group. $n = 4$ independent samples. All statistical analyzes were performed by one-way ANOVA, data represent mean ± standard deviation, $^{**}p < 0.01$, $^{***}p < 0.001$.

Verification of BioES-suture in accelerating wound healing in vivo

To evaluate the therapeutic effect of BioES-suture in vivo, we used Sprague-Dawley rats as the animal model. BioES-suture was used to treat bleeding muscle incisions of rats, promoting injury repair through tight suturing as well as ES action (Fig. 4a). The other two groups were treated with bioabsorbable suture (Bio-suture) and no suture (control). To further understand the role of ES on muscle repair, we measured electromyographic (EMG) signals in the three groups (Supplementary Fig. 18a, Supplementary Movie S2). The results showed that the intervention of ES significantly elevated the signal intensity of EMG, while the signal intensity was basically the same in the Bio-suture and control groups (Fig. 4b and Supplementary Fig. 18b). This demonstrated that BioES-suture generated electrical stimulation under the mechanical movement state, which activated calcium signaling (VGCC) and triggered Ca^{2+} influx via voltage-gated ion channels[44], thus generating stronger EMG signals and promoting cellular secretion of endogenous growth factors (Supplementary Fig. 19 and Supplementary Note 2). The recovery was observed by detaching the sutures and extracting traumatized muscles of the three groups after 10 days (Fig. 4c). The muscles of the control group showed an abnormal blood-red color, indicating that the muscle tissue was severely infected. indicating that the wound had been tightened by the sutures to halt the bleeding.

To further confirm the efficacy of BioES-suture in the wound regeneration and tissue remodeling processes, we stained the muscle trauma tissues of the three groups with hematoxylin eosin (H&E) and Masson trichrome (Masson) (Fig. 4d). As the results showed that there were still muscle deficiencies on the traumas of the control and Bio-suture groups, especially the control group still had clear scratches. Compared with the other two groups, BioES-suture improved tissue migration from the wound bed, with faster wound regeneration and almost complete wound healing throughout the experiment, which was consistent with the scratch assay in vitro. In Masson staining, collagen deposition was evident in the BioES-suture group, with most of the reconstruction being normal muscle, indicating that it was in the remodeling phase of the normal wound healing process. In addition, the healed muscle tissue in the BioES-suture group did not show significant fibrosis, whereas the Bio-suture group proliferated fibrotic tissue (Supplementary Note 3). The wound closure was compared with the original size of the wound (Fig. 4f). The wound closure rates (%) were 60.4%, 82.2% and 96.5% for the control, Bio-suture, and BioES-suture groups, respectively. These results confirm the effectiveness of BioES-suture in promoting tissue regeneration and repair for acute wounds and the applied electrical stimulation could reduce the tendency of fibrosis in the healed tissue to some extent.

To understand the changes in cellular metabolism during the recovery period of muscle wounds, we investigated a variety of growth factors associated with wound healing, including EGF, TGF-β and VEGF-A. The distribution of these key growth factors was assessed by immunohistochemistry (IHC) (Fig. 4e). IHC staining images showed the overall expression distribution of the various growth factors, indicated in dark brown color. In general, the IHC results indicated significantly enhanced secretion of EGF, TGF-β and VEGF-A in the BioES-suture group compared to the other two groups. Integrated optical density (IOD) curve analysis was subsequently performed to quantify the intensity of growth factor expression (Fig. 4g). The average IOD of EGF, TGF-β and VEGF-A in the BioES-suture group was 0.41, 0.39 and 0.33, respectively, which was higher than that in the Bio-suture group (0.30, 0.32 and 0.29) and the control group (0.25, 0.27 and 0.22). In addition, the expression of the three growth factors was higher in the Bio-suture group than that of the control group, suggesting that mechanical regulation could also promote tissue regeneration as well as play an essential role in angiogenesis and healing metabolism. These findings illustrate that the electromechanical synergistic effects of BioES-suture have a more extraordinary ability to remodel new tissue and accelerate healing metabolism for effective wound healing.

Intervention mechanisms and recovery evaluation of wound repair

The mechanism of accelerated wound healing by BioES-suture intervention was exploited. Immunofluorescence (Supplementary Fig. 20, 21 and 22) and real-time quantitative polymerase chain reaction (RT-qPCR) of healing muscle tissue (Supplementary Fig. 23) further revealed higher expression levels of the three growth factors in the BioES-suture group. Simultaneously, the phosphorylation levels of PI3K, ERK, and Akt were elevated in the BioES-suture group (Supplementary Fig. 24, 25, and 26), which was attributed to the fact that electrical stimulation elevated the expression of growth factors and thus increased the phosphorylation of downstream Shc-Grb-Sos complex and PI3K to enhance the phosphorylation levels of ERK and Akt[45]. Moreover, RT-qPCR of fibroblasts further showed the regulation of three growth factor secretion by calcium channels, suggesting that electrical stimulation may promote tissue repair by affecting the opening of calcium channels to enhance expression of relevant growth factors (Supplementary Note 2). Therefore, the mechanism of accelerated wound healing by BioES-suture could be summarized in the following two aspects: firstly, BioES-suture generates an applied electric field along the direction of the endogenous electric field for electrical stimulation (Supplementary Note 4), which enhances the secretion of the three growth factors at the wound site (Fig. 5a). Secondly, the enhanced expression of growth factors in response to electrical stimulation upregulated the PI3K/Akt/mTOR and MAPK signaling pathways, thereby promoting cell migration, proliferation and extracellular matrix (ECM) deposition to accelerate wound healing (Fig. 5b).

Subsequently, we assessed the status of wound healing. Angiogenesis and inflammatory cell infiltration were verified in vivo using CD31/α-smooth muscle actin (α-SMA) and CD3/CD20 immunofluorescence staining. Immunofluorescence staining of α-SMA-positive (green) and CD31-positive (red) tissues showed that angiogenic areas were significantly enhanced in the BioES-suture group compared to the other groups (Fig. 5c). The percentage of CD31- or α-SMA-positive areas were highest in the BioES-suture group, suggesting an increased level of vessel formation during the healing period (Fig. 5d). Double immunofluorescence staining by t-cells marked CD3 (red fluorescence) and b-cells marked CD79α (green fluorescence) revealed that BioES-suture group had less inflammation infiltration of the healing muscle tissues than the other groups (Fig. 5e and Supplementary Fig. 27). In particular, the infiltration of t-cells and b-cells decreased by 85.4% and 73.7%, respectively, compared with the control group. These results indicated that the BioES-suture group passed through the inflammatory phase faster than the other groups and rapidly transitioned to the migration and remodeling phase.

Furthermore, we established a rat infected wound model to validate the antimicrobial properties of BioES-suture. The wounds were stitched with ordinary surgical sutures and BioES-suture, respectively (Supplementary Fig. 28a). After one week, we observed the wound healing outcomes and collected wound tissues for bacterial culture and counting. We found that compared to wounds stitched with ordinary surgical sutures, those stitched with BioES-suture exhibited better healing outcomes, with significantly lower bacterial culture counts in the wound tissues. To compare with other clinical methods for preventing postoperative infections, we created another batch of rat models using the same approach. We employed one of the most common measures for postoperative infection prevention-wound disinfection-by disinfecting the wounds daily. After one week, we observed the wound healing outcomes and quantified the bacteria in the wound tissues. We found that in rats treated with BioES-suture, even without daily wound disinfection, the bacterial count in the infected tissue remained at a low level, comparable to the bacterial count in the wound tissue of rats sutured with ordinary sutures and subjected to daily wound disinfection (Supplementary Fig. 28b). This indicated that BioES-suture could effectively reduce the severity of postoperative infections, thereby reducing the risk of postoperative infections.

Discussion

In conclusion, we present a bioabsorbable electrical stimulation suture (BioES-suture) that accelerates muscle gashes healing by converting the mechanical energy of movement into effective electrical stimulation. The suture was mechanically tested to exhibit sewing strength up to the standard of commercial sutures. Simultaneously, the modified melt-spinning allowed the sheath to tightly encapsulate the pre-assembled core fiber, enabling BioES-suture to produce a sensitive electrical output during the healing period. Therapeutic experiments in vivo and in vitro have demonstrated that the suture can generate the endogenous electric field at the wound for electrical stimulation, thereby promoting cell proliferation and migration to accelerate wound repair and reduce the risk of infection. In addition, the component units of BioES-suture are fabricated from biocompatible and biodegradable materials, and can be safely applied to suture in vivo without the need for secondary surgical removal. Therefore, BioES-suture is expected to be applied to other injuries in vivo other than muscle wounds, further boosting the development of biomedical field.

Methods

Materials

Mg filament (200 μm) was bought from Suzhou JingJun Materials Technology Co. Ltd., China. Poly(lactic-co-glycolic acid) (PLGA, 75:25) masterbatch was purchased from Nature Works, USA. Polycaprolactone (PCL, $M_w = 45000$ g/mol) masterbatch was purchased from Shanghai Macklin Biochemical Technology Co. Ltd., China. Hexafluoroisopropanol (HFIP) was purchased from Shanghai Aladdin Reagent Co. Ltd., China.

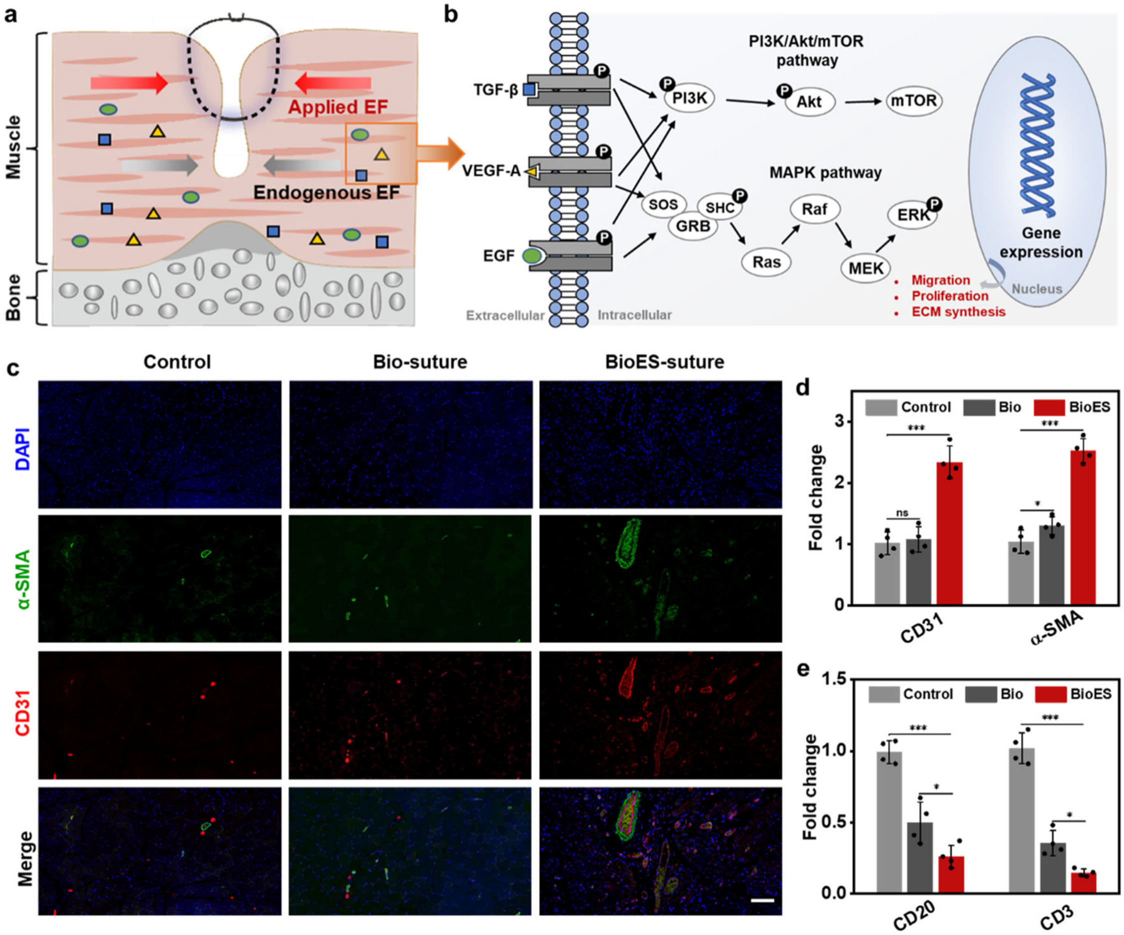

Fig. 5 | Intervention mechanisms and recovery evaluation of wound repair. **a** Wound-healing mechanism between endogenous EF and applied EF. **b** Electrical stimulation activates PI3K/Akt/mTOR and MAPK signaling pathways, which promotes cell migration and proliferation to accelerate wound healing. **c** Immunofluorescence observation and quantification **d** of CD31 and α-SMA staining in each group. CD31 and α-SMA both indicated increased angiogenesis. Scale bar: 100 μm. $n = 4$ independent samples. **e** Quantification of CD20 and CD3 positive signals, biomarkers of B and T cells, respectively, at the wound areas in each group. $n = 4$ independent samples. All statistical analyzes were performed by one-way ANOVA, data represent mean ± standard deviation, $^{*}p < 0.05$, $^{**}p < 0.01$, $^{***}p < 0.001$.

Fabrication of biodegradable electrical stimulation suture

First, for preparation of PLGA precursor solution, PLGA masterbatch was dissolved in HFIP with 12 wt% at 60 °C and stirred for 20 min to obtain a uniform spinning solution. Second, using the Fermat spinning equipment (TFS-700, Beijing Xinrui Baina Technology Co., Ltd., China) to fabricate PLGA nanofibers. The applied positive and negative voltage were 8 ± 0.5 kV, the distance between positive and negative poles of the needle (inner diameter 0.5 cm) was 16 cm, and the feed rate of spinning solution was 0.015 mL/h. The rotating speed of metal funnel was 400 rpm, and the winder roller was rotated at 11 rpm. The PLGA nanofibers were twisted around the Mg filament to produce the pre-assemble core fiber (Mg@PLGA). Third, the fabrication of PCL sheath was performed by modified melt-spinning. Before processing, the PCL masterbatch was as placed in an oven (50 °C) for 4 h for removing the moisture. At a processing temperature of about 90 °C, the pre-assembled core fiber was drafted into the PCL melt and drawn from the spinning needle at a drafting rate of 3 m/min. After cooling, the bioabsorbable passive electrical stimulation suture (BioES-suture) was obtained.

Characterization of structure, physical and electrical properties, and degradation behavior of BioES-suture

The morphologies of BioES-suture were observed using an ultra-depth-of-field microscope (Leica DVM6, Germany) and scanning electron microscopy (Hitachi SU8000, Japan). Mechanical properties were measured with an electronic universal testing machine (Instron 5969, from Instron Corporation, USA) at a tensile rate of 100 mm/min.

The Keithley 6514 (from Keithley Instruments, USA) and oscilloscope (Keysight DSOX3012T, USA) were used to test the electrical output performance of BioES-suture in vitro and in vivo. The process in vitro is as follows: BioES-suture was wrapped around an artificial muscle fiber and its ends were fixed on a stretching machine (Yangyi Machinery Manufacturing Co. Ltd., China). The stretcher enables the adjustment of different stretching ratios to accurately measure the electrical signals at different levels of contraction. Then, it was placed in different media and measured by stretch-recovery cycle. The process in vivo is as follows: BioES-suture was stitched into the leg muscles of rats with one end of the suture exposed and connected to an oscilloscope, and the electrical output of BioES-suture induced by contraction-diastole of the muscle was measured during the normal activity of the rats.

Kelvin probe force microscopy (Park NX20, South Korea) was applied to measure the surface potential of PCL film before and after contacting PLGA nanofibers membrane. PCL film was formed by spreading the PCL melt in a polytetrafluoroethylene mold and cooled, and PLGA nanofiber membrane was prepared by using an electrospinning machine (TEADFS-700, China).

FEM simulations of the electric field which was generated at the suture wound were performed using COMSOL Multiphysics. Firstly, a three-dimensional muscle suture model was modeled by COMSOL software. Then, electrical parameters (Supplementary Table 2) were set for different tissues or materials. After electrical field simulation calculation, the electric field intensity across BioES-suture and wounds was obtained.

The in vitro degradation behavior of BioES-suture was studied using a thermostatic shaking incubator (HZQ-F100, China) with the following conditions: PBS buffer (pH = 7.4), 37 °C, 150 rpm. Fresh PBS was changed every three days.

Cell culture

NIH 3T3 fibroblasts (Chinese Academy of Science Cell Bank, Shanghai, China) were cultured in Dulbecco's modified eagle high glucose medium (DMEM-HG, Gibco, USA) supplemented with 10% fetal bovine serum (FBS, Gibco, USA) and 1 % penicillin/streptomycin (Gibico, USA). L929 fibroblasts (Chinese Academy of Science Cell Bank, Shanghai, China) were cultured in DMEM-HG medium containing 10 % FBS and 1 % penicillin/streptomycin. The cell culture conditions were humid incubator with 5% CO_2 at 37 °C.

Biocompatibility test

All materials of BioES-suture were tested for biocompatibility. The L929 fibroblasts were seeded into 96-well plates, 200 µL per well, and placed in a constant temperature incubator for 24 h. After removing the culture medium, three sutures (Mg filament, Mg@PLGA fiber and BioES-suture) were cut into 1 cm segments, and cells in different wells were separately added different sutures. At specific time points (1 day, 3 days or 7 days), 22 µL of Cell Counting Kit-8 (CCK-8, Solarbio, China) was added to the wells to be tested, and then incubated at 37 °C for 1 h. The absorbance was measured at 450 nm to assess cell activity according to the optical density (OD) values. The biocompatibility of BioES-suture on L929 fibroblasts was also tested with Live/Dead staining. Briefly, at the above specific time points, Live/Dead staining solutions were added to the samples to be tested, and then these samples were observed under a fluorescence microscope (BX-51, Japan) after incubation for 15 min. Moreover, the degradation solutions of Mg and BioES-suture were added to the cell culture medium, and after 24 h of incubation, Calcein/PI staining was employed to distinguish live cells from dead cells to measure the biocompatibility of the degradation products.

Scratch assay

The NIH 3T3 fibroblasts were cultured in 6-well cell plate for 48 h. The BioES-suture was wound around an artificial muscle fiber to generate electricity through the stretch-recovery cycles (simulating contraction-diastole of muscle). The other end of the suture was placed on the bottom of a six-well plate containing NIH 3T3 fibroblasts for electrical stimulation. Thereafter, a scratch about 500 µm wide was made on the fibroblasts that covered the 6-well cell plate using the tip of the pipette. The cells are intervened under different conditions. The fibroblasts were treated by the 2.5 V ES generated by BioES-suture. The ES were performed for 1 h at 12 h intervals.

Cell proliferation test

The NIH 3T3 fibroblasts (ATCC, CRL-1658) were cultured in 12-well cell plate for 24 h. The 12-well cells were randomly assigned to two groups, namely control group and ES group. The fibroblasts in control group received no intervention. The fibroblasts were treated with the BioES-suture at voltage of 2.5 V in the ES group. The fibroblasts of ES group were stimulated for 1 h at 12 h intervals. After 72 h of incubation in the cell culture incubator, cells were washed three times with PBS and fixed with 4% paraformaldehyde (Sangon Biotech, China) at room temperature for 20 min. The cells were then permeabilized with 0.05% Triton X-100 (Sangon Biotech, China) for 10 minutes and blocked with 10% BSA (Solarbio, China) for 30 min. Subsequently, the cells were incubated overnight at 4 °C with rabbit anti-Ki-67 antibody (1:400, Abcam). On the following day, unbound antibodies were washed off by rinsing the cells three times for 10 min each with PBS. The cells were then incubated with Goat Anti-Rabbit IgG H&L (Alexa Fluor® 488) (1:500, Abcam) at room temperature for 1 h. Ki67 was used for immunofluorescence staining and quantified the proportion of Ki67-positive cells and the relative fluorescence intensity of Ki67 in each group. Finally, DAPI (Sigma-Aldrich, USA) was applied to label nuclei and preserve fluorescence. All images were acquired using a confocal microscope (LSM 710, ZEISS, Germany). The percentage of Ki-67 positive cells was determined by randomly counting five fields of view. At least 500 $DAPI^+$ positive cells were analyzed using Image J software (NIH, Bethesda, MD, USA). CCK-8 was used to assess the viability of NIH 3T3 fibroblasts at different time points.

ELISA assay

For EGF, TGF-β, VEGF-A ELISA tests (Abcam, UK), samples were collected from cell culture supernatant at various time points (1 day, 2 days or 3 days). All ELISA tests were performed according to protocols recommended by vendors. The absorbance at 450 nm was measured by microplate readers.

Bacterial Live/Dead assay

Staphylococcus aureus (S. aureus, ATCC 43300) and Escherichia coli (E. coli, ATCC 25922) were cultured in tryptic soy broth (TSB) medium for 24 h at 37 °C. Each bacterial culture was divided into three groups, where ordinary surgical sutures, BioES-suture and electricity-producing BioES-suture were immersed in the respective cultures. After incubation at 37 °C for 6 h, the sutures were removed and washed twice with PBS. The sutures were then stained in the dark for 30 min with a Live/Dead™ BacLight™ Bacterial Viability Kit (Invitrogen, USA) containing propidium iodide (PI, 3 µL/mL) and Syto-9 (1:1). The stained sutures were placed on microscope slides, and the fluorescence of live and dead bacteria was observed using a fluorescence microscope (Ts2R, Nikon, Japan). The fluorescence intensity of dead bacteria was measured using Image J software (NIH, Bethesda, MD, USA).

Animal experiment

All animal experiments were performed according to protocols approved by approved by Committee on Ethics of Donghua University (DHUEC-NSFC-2022-43). Purchased from SiPeiFu Biotechnology Co., LTD (Suzhou, China), twelve six-eight-weeks-old Sprague-Dawley female rats with an average weight of 250–300 g were kept in a certified animal facility. Mice were group-housed if same sex little-mates were available. All the samples were sterilized by UV before initiating the experiments.

In vivo therapeutic test

Female Sprague–Dawley rats were selected for the rat experiments. They were anesthetized with isoflurane inhalation (1.5 L/min). The leg hair of rats was removed with an electrical hair cutter. A scalpel was used to cut the skin of the thigh area of the rats to expose the muscles. The muscle was then incised with a linear bleeding incision of 2 cm in length and 0.5 cm in depth. The muscle wounds were divided into three groups treated with different conditions: untreated (control), bioabsorbable suture (Bio-suture) and BioES-suture. Three stitches were performed in the muscle wound of the suture group. Skin wounds in all groups were closed using normal commercial sutures. During 14 days of treatment, the electromyography (EMG) signals were recorded with time by Neusen.U16 (Changzhou Boruikang Technology Co. Ltd., China).

Histology evaluation

After 10 days of recovery, digital photographs of each wound were captured with sutures removed to analyze the wound healing. Muscle wounds were removed and immersed in a 10 % formalin solution, the wound tissue with surrounding un-wounded muscle was fixed. The samples then underwent a general procedure (dehydration, clearing, and embedding) for histopathological analysis. Paraffin sections with 4 µm thickness were processed with H&E and Masson stain. Histology images were collected on an inverted optical microscope. Image J was used to measure areas of the wounds and to analyze the positive expressions. Wound healing rate (%) = (wound area at day 0 − wound area remaining wound)/(wound area at day 0) × 100 %.

Immunofluorescence staining

Serial tissue sections were processed according to the standard immunofluorescence staining procedures, including deparaffinization, antigen-retrieval (citrated buffer, heat-induced), permeabilization (0.3% Triton PBST), and antigen blocking (goat serum, Cell Signaling Technology, USA). Then, as-prepared sections were incubated with antibodies, including mouse monoclonal α-SMA primary antibody (1:200; Novus Biologicals, USA), rabbit polyclonal CD31 primary antibody (1:200; Abcam, UK), rabbit monoclonal CD3 primary antibody (1:200; Abcam, UK), and mouse monoclonal CD79A primary antibody (1:200; Santa Cruz Biotechnology, USA). Then the sections were PBST-washed twice and incubated with secondary antibodies (goat anti-mouse Alexa 488, donkey anti-rabbit Alexa 555, Thermo Fisher) at room temperature before counterstaining with DAPI. Fluorescent images were captured via Zeiss Axio Observer 5 Inverted Phase Contrast Fluorescent Microscope. Fluorescence intensity was analyzed and calculated using Image J ($n = 4$/group).

Calcium imaging

The changes in intracellular Ca^{2+} concentration were evaluated using the calcium probe Fura-4 AM. The cells were stained for 30 min at 37 °C with the probe (working concentration 3 μM) dissolved in Hank's balanced salt solution. Rat cardiac muscle cells were dissociated from neonatal rats (P0-2). Images were acquired on a confocal microscope (LSM 710, ZEISS, Germany) with a 20× objective for long-term imaging of live cells. Time series images were acquired every 2 s for 200 cycles, with a spatial resolution of 512 × 512 pixels over approximately 430 s. The fluorescence intensity changes over time for each cell's region of interest (ROI) and background were extracted using Image J software (Bethesda, MD, USA). In the calcium signal data presented in this study, relative fluorescence changes ($\Delta F/F_0$) were used. $\Delta F/F_0 = (F - F_0)/F_0$, where F is the current fluorescence intensity of the ROI, and the baseline fluorescence value F_0 is the average of the lowest 25% of all fluorescence signals.

Real-time quantitative polymerase chain reaction (RT-qPCR) assay

For in vitro experiments, NIH 3T3 fibroblasts were seeded into culture plates and divided into three groups: control group, BioES-suture group, and BioES-suture+Verapamil group. After 24 h of cultivation, the groups were treated under different conditions: no additional treatment, treatment with BioES-suture, and treatment with BioES-suture combined with verapamil (10 μM). After three days of treatment, the cells were prepared for subsequent experiments. For in vivo experiments, rats were divided into two groups. After making surgical incisions, the wounds were closed using either ordinary surgical sutures or BioES-suture. One week later, the rats were sacrificed, and tissues surrounding the wound were collected for subsequent experiments. Total RNA was extracted from the cells and tissues according to the protocol provided by the supplier (EZBio-science, USA). First-strand cDNA was synthesized using the HiScript III All-in-one RT SuperMix Perfect for qPCR kit (Vazyme, China) following the manufacturer's instructions. The following qPCR reactions were performed using the ChamQ Universal SYBR qPCR Master Mix kit (Vazyme, China) in ABI PRISM 9700 PCR machine (ABI, USA). Each RT-qPCR reaction was conducted in quadruplicate. The resulting CT values were normalized to Gapdh (internal control) using the 2-ΔΔCT method to analyze the relative quantification of gene expression. RT-qPCR primer sequences are provided in Supplementary Table 3 of the supporting information.

Infected wound model creation

Female Sprague-Dawley rats (8 weeks old, 200–300 g) were used for the experiment. After anesthesia, a 3 cm incision was made on the back of each rat, and the wound was inoculated with 1 mL of S.aureus suspension (1×10^8 CFU/mL). Two days post-surgery, the wounds showed signs of redness and swelling. The wounds were then sutured with either ordinary surgical sutures or BioES-suture. The rats were divided into two groups, each containing six rats, with three rats sutured using ordinary surgical sutures and three rats sutured using BioES-suture. One group of rats underwent routine feeding and daily activity monitoring, while the other group, in addition to routine care, had their wounds disinfected daily with povidone-iodine. All animals had free access to water and food. After one week, the wound healing outcomes were observed. The rats were euthanized using an overdose of anesthesia, and a 2 cm × 1 cm tissue sample was excised from the incision site. Under sterile conditions, the tissue was minced and homogenized in 1 mL of PBS. A 100 μL of the supernatant were serially diluted 1000-fold and evenly spread onto agar culture plates. The plates were incubated at 37 °C for 24 h, after which bacterial colonies were counted.

Statistical analysis and reproducibility

At least three independent experiments of each type have been done and produced consistent results. All analysis data were expressed as mean ± standard deviation (at least three or more independent sample). The statistical difference among different groups was accessed via one-way analysis of variance (ANOVA) methods. Image J, Origin 2018b and Excel were used for data analysis and plotting. Differences of $^{*}p < 0.05$ denote significance, while differences of $^{**}p < 0.01$ and $^{***}p < 0.001$ denote high significance compared with other groups.

Reporting summary

Further information on research design is available in the Nature Portfolio Reporting Summary linked to this article.

Data availability

All data supporting the findings of this study are available within the article and its Supplementary files. Any additional requests for information can be directed to, and will be fulfilled by, the corresponding authors. Source data are provided with this paper.

References

1. Rodrigues, R. R., Carmona, M. J. C. & Junior, J. O. C. A. Bleeding and damage control surgery. *Curr. Opin. Anesthesio.* **29**, 229–233 (2016).
2. Childs, D. R. & Murthy, A. S. Overview of wound healing and management. *Surg. Clin. N. Am.* **97**, 189–207 (2017).
3. Wang, L. et al. Hierarchical helical carbon nanotube fibre as a bone-integrating anterior cruciate ligament replacement. *Nat. Nanotechnol.* **18**, 1085–1093 (2023).
4. Wang, L. et al. High-performance artificial ligament made from helical polyester fibers wrapped with aligned carbon nanotube sheets. *Adv. Healthc. Mater.* **12**, 2301610 (2023).

5. Gracey, E. et al. Tendon and ligament mechanical loading in the pathogenesis of inflammatory arthritis. *Nat. Rev. Rheumatol.* **16**, 193–207 (2020).
6. Holmes, G. et al. Single-cell analysis identifies a key role for Hhip in murine coronal suture development. *Nat. Commun.* **12**, 7132 (2021).
7. Kalidasan, V. et al. Wirelessly operated bioelectronic sutures for the monitoring of deep surgical wounds. *Nat. Biomed. Eng.* **5**, 1217–1227 (2021).
8. Research highlights. *Nature* **617**, 654 (2023).
9. Ma, Z. et al. Bioinspired tough gel sheath for robust and versatile surface functionalization. *Sci. Adv.* **7**, eabc3012 (2021).
10. Saghazadeh, S. et al. Drug delivery systems and materials for wound healing applications. *Adv. Drug Deliv.Rev.* **127**, 138–166 (2018).
11. Wang, X., Ge, J., Tredget, E. E. & Wu, Y. The mouse excisional wound splinting model, including applications for stem cell transplantation. *Nat. Protoc.* **8**, 302–309 (2013).
12. Mostafalu, P. et al. A toolkit of thread-based microfluidics, sensors, and electronics for 3D tissue embedding for medical diagnostics. *Microsyst. Nanoeng.* **2**, 16039 (2016).
13. Yao, G. et al. Effective weight control via an implanted self-powered vagus nerve stimulation device. *Nat. Commun.* **9**, 5349 (2018).
14. Li, T. et al. Cell activity modulation and its specific function maintenance by bioinspired electromechanical nanogenerator. *Sci. Adv.* **7**, eabh2350 (2021).
15. Kim, D. H. et al. Thin, flexible sensors and actuators as 'instrumented' surgical sutures for targeted wound monitoring and therapy. *Small* **8**, 3263–3268 (2012).
16. Zheng, Q., Tang, Q., Wang, Z. L. & Li, Z. Self-powered cardiovascular electronic devices and systems. *Nat. Rev. Cardiol.* **18**, 7–21 (2021).
17. Zhang, S. et al. Leveraging triboelectric nanogenerators for bioengineering. *Matter* **4**, 845–887 (2021).
18. Shi, B., Li, Z. & Fan, Y. Implantable energy-harvesting devices. *Adv. Mater.* **30**, 1801511 (2018).
19. Nain, A. et al. Progress in the development of piezoelectric biomaterials for tissue remodeling. *Biomaterials* **307**, 122528 (2024).
20. Khan, A. et al. Piezoelectric and triboelectric nanogenerators: promising technologies for self-powered implantable biomedical devices. *Nano Energy* **119**, 109051 (2024).
21. Yao, S. et al. Implantable, biodegradable, and wireless triboelectric devices for cancer therapy through disrupting microtubule and actins dynamics. *Adv. Mater.* **35**, 2303962 (2023).
22. Vinikoor, T. et al. Injectable and biodegradable piezoelectric hydrogel for osteoarthritis treatment. *Nat. Commun.* **14**, 6257 (2023).
23. Jin, F. et al. Biofeedback electrostimulation for bionic and long-lasting neural modulation. *Nat. Commun.* **13**, 5302 (2022).
24. Snigdha, R. et al. A self-powered multifunctional dressing for active infection prevention and accelerated wound healing. *Sci. Adv.* **9**, eadc8758 (2023).
25. Meng, X. et al. An ultrasound-driven bioadhesive triboelectric nanogenerator for instant wound sealing and electrically accelerated healing in emergencies. *Adv. Mater.* **35**, 2209054 (2023).
26. Yang, Y. et al. Improved pharmacodynamics of epidermal growth factor via microneedles-based self-powered transcutaneous electrical stimulation. *Nat. Commun.* **13**, 6908 (2022).
27. Zhou, M. et al. Contact separation triboelectric nanogenerator based neural interfacing for effective sciatic nerve restoration. *Adv. Funct. Mater.* **32**, 2200269 (2022).
28. Lee, D.-M. et al. An on-demand bioresorbable neurostimulator. *Nat. Commun.* **14**, 7315 (2023).
29. Liu, Y. et al. Exercise-induced piezoelectric stimulation for cartilage regeneration in rabbits. *Sci. Transl. Med.* **14**, eabi7282 (2022).
30. Yao, G. et al. A self-powered implantable and bioresorbable electrostimulation device for biofeedback bone fracture healing. *Proc. Natl. Acad. Sci.* **118**, e2100772118 (2021).
31. Jin, F. et al. Physiologically self-regulated, fully implantable, battery-free system for peripheral nerve restoration. *Adv. Mater.* **33**, 2104175 (2021).
32. Ouyang, H. et al. Symbiotic cardiac pacemaker. *Nat. Commun.* **10**, 1821 (2019).
33. Yang, W. et al. Self-powered interactive fiber electronics with visual-digital synergies. *Adv. Mater.* **33**, 2104681 (2021).
34. Gong, W. et al. Continuous and scalable manufacture of amphibious energy yarns and textiles. *Nat. Commun.* **10**, 868 (2019).
35. Zhang, D. et al. Abrasion resistant/waterproof stretchable triboelectric yarns based on fermat spirals. *Adv. Mater.* **33**, 2100782 (2021).
36. Li, C. et al. Design of biodegradable, implantable devices towards clinical translation. *Nat. Rev. Mater.* **5**, 61–81 (2020).
37. Li, W. et al. Biodegradable materials and green processing for green electronics. *Adv. Mater.* **32**, 2001591 (2020).
38. Choi, Y. S. et al. Stretchable, dynamic covalent polymers for soft, long-lived bioresorbable electronic stimulators designed to facilitate neuromuscular regeneration. *Nat. Commun.* **11**, 5990 (2020).
39. Gong, W. et al. Scalable and reconfigurable green electronic textiles with personalized comfort management. *ACS Nano* **16**, 12635–12644 (2022).
40. Wang, L. et al. A fully biodegradable and self-electrified device for neuroregenerative medicine. *Sci. Adv.* **6**, eabc6686 (2020).
41. Lee, G. M. et al. A bioresorbable peripheral nerve stimulator for electronic pain block. *Sci. Adv.* **8**, eabp9169 (2022).
42. Jun, I. et al. Synergistic stimulation of surface topography and biphasic electric current promotes muscle regeneration. *Bioact. Mater.* **11**, 118–129 (2022).
43. Wang, C. et al. Flexible patch with printable and antibacterial conductive hydrogel electrodes for accelerated wound healing. *Biomaterials* **285**, 121479 (2022).
44. Park, J. et al. Imperceptive and reusable dermal surface EMG for lower extremity neuro-prosthetic control and clinical assessment. *npj Flex. Electron.* **7**, 49 (2023).
45. Luo, R. et al. Reshaping the endogenous electric field to boost wound repair via electrogenerative dressing. *Adv. Mater.* **35**, 2208395 (2023).

Acknowledgements

We gratefully acknowledge the financial support by National Natural Science Foundation of China (No. 52073057, No. 82072552 and No. 82301331), the Fundamental Research Funds for the Central Universities (2232024Y-01), DHU Distinguished Young Professor Program (LZA2023001) and Shanghai Pujiang Program (22PJD050).

Author contributions

C.Y.H., H.Z.W., H. W., and L.P.L guided the project. H.Z.W., C.Y.H., Z.Q.S, and Y.F.J. conceived the idea and designed the experiment. Z.Q.S. fabricated the BioES-suture. Z.Q.S, Y.F.J., J.B.L., Y.D., and Y.Q. performed the experiments and measurements. H.B.S, S.K.Y., and H.W. guided the biomolecular mechanism. Y.L., C.Y.H., Y.G.L., Q.H.Z., and K.R.L. revised the manuscript. All authors analyzed the experimental data, drew the figures and prepared the manuscript. All authors discussed the results and reviewed the manuscript.

Competing interests

The authors declare no competing interests.

Additional information

Supplementary information The online version contains supplementary material available at https://doi.org/10.1038/s41467-024-52354-x.

Correspondence and requests for materials should be addressed to Linpeng Li, Hongzhi Wang, Hui Wang or Chengyi Hou.

Peer review information *Nature Communications* thanks Zong-Hong Lin, and the other, anonymous, reviewer(s) for their contribution to the peer review of this work. A peer review file is available.

Reprints and permissions information is available at http://www.nature.com/reprints